



HAL
open science

High contrast at small separation – II. Impact on the dark hole of a realistic optical set-up with two deformable mirrors

Mathilde Beaulieu, P Martinez, L Abe, C Gouvret, P Baudoz, R Galicher

► To cite this version:

Mathilde Beaulieu, P Martinez, L Abe, C Gouvret, P Baudoz, et al.. High contrast at small separation – II. Impact on the dark hole of a realistic optical set-up with two deformable mirrors. Monthly Notices of the Royal Astronomical Society, 2020, 498 (3), pp.3914-3926. 10.1093/mnras/staa2106 . hal-02962419

HAL Id: hal-02962419

<https://hal.science/hal-02962419>

Submitted on 12 May 2023

HAL is a multi-disciplinary open access archive for the deposit and dissemination of scientific research documents, whether they are published or not. The documents may come from teaching and research institutions in France or abroad, or from public or private research centers.

L'archive ouverte pluridisciplinaire **HAL**, est destinée au dépôt et à la diffusion de documents scientifiques de niveau recherche, publiés ou non, émanant des établissements d'enseignement et de recherche français ou étrangers, des laboratoires publics ou privés.

High contrast at small separation – II. Impact on the dark hole of a realistic optical set-up with two deformable mirrors

M. Beaulieu,¹★ P. Martinez,¹ L. Abe,¹ C. Gouvret,¹ P. Baudoz² and R. Galicher²

¹Université Côte d’Azur, Observatoire de la Côte d’Azur, CNRS, Laboratoire Lagrange, F-06108 Nice, France

²LESIA, Observatoire de Paris, PSL Research University, CNRS, Sorbonne Universités, UPMC Univ. Paris 06, Univ. Paris Diderot, Sorbonne Paris Cité, 92195 Meudon, France

Accepted 2020 July 14. Received 2020 July 13; in original form 2020 March 18

ABSTRACT

Future large space- or ground-based telescopes will offer the resolution and sensitivity to probe the habitable zone of a large sample of nearby stars for exo-Earth imaging. To this end, such facilities are expected to be equipped with a high-contrast instrument to efficiently suppress the light from an observed star to image these close-in companions. These observatories will include features such as segmented primary mirrors, secondary mirrors, and struts, leading to diffraction effects on the star image that will limit the instrument contrast. To overcome these constraints, a promising method consists in combining coronagraphy and wavefront shaping to reduce starlight at small separations and generate a dark region within the image to enhance the exoplanet signal. We aim to study the limitations of this combination when observing short-orbit planets. Our analysis is focused on SPEED, the Nice test bed with coronagraphy, wavefront shaping with deformable mirrors (DMs), and complex telescope aperture shape to determine the main realistic parameters that limit contrast at small separations. We develop an end-to-end simulator of this bench with Fresnel propagation effects to study the impact of large phase and amplitude errors from the test-bed optical components and defects from the wavefront shaping system on the final image contrast. We numerically show that the DM finite stroke and non-functional actuators, coronagraph manufacturing errors, and near-focal-plane phase errors represent the major limitations for high-contrast imaging of exoplanets at small separations. We also show that a carefully defined optical set-up opens the path to high contrast at small separation.

Key words: instrumentation: miscellaneous – techniques: high angular resolution – techniques: miscellaneous – methods: numerical – planetary systems.

1 INTRODUCTION

So far, more than 4000 exoplanets have been discovered,¹ and only ~40 have been directly detected with masses greater than the mass of Jupiter, showing the difficulty of revealing Earth-like exoplanets in the habitable zone (defined as the liquid water zone). Direct detection enables detailed characterization and in particular remote sensing of their atmospheres, opening the path to searching for habitability features. Space-based telescopes, limited in size but free of atmospheric turbulence, should reach the contrast level required to image the reflected light of habitable planets around bright stars (A, F, or G types). Thermal emission of Earth-like planets should be directly imaged with ground-based extremely large telescopes (ELTs, large primary mirrors but affected by the Earth’s atmosphere) around M-stars (fainter stars with closer habitable zones). Despite atmospheric considerations, those two complementary methods share the common challenge of developing instruments that provide high contrast at small angular separations. The large UV–optical–infrared (LUVOIR, Bolcar et al. 2018; Pueyo et al. 2019; Juanola-Parramon et al. 2019b) and the habitable exoplanet observatory (HABeX, Gaudi

et al. 2018; Krist et al. 2019) spatial mission concepts, for instance, aim to achieve a contrast ratio of 10^{-10} at $2 \lambda/D$ (with λ defining the wavelength and D the telescope aperture diameter) to detect Earth-like planets around bright stars. Their ground-based counterparts are expected to detect Earth-like planets around M-stars if instruments achieve contrast ratios of 10^{-8} at $1 \lambda/D$ (Guyon et al. 2012).

High-contrast imaging instrumentation and observation techniques have to face various challenges: (1) unfriendly pupil shape (primary mirror central obscuration, segmentation, etc.) that degrades the contrast ratio; (2) a small-angular-separation regime where a large amount of the on-axis point-spread function (PSF) is concentrated; and (3) dynamic, static, and quasi-static aberrations due to environmental instabilities (changes of temperature, pressure, and gravity induce deformations in the structure and mirrors, vibrations, etc.) that significantly degrade the performance. High-contrast imaging requires multiple-step corrections such as extreme-adaptive optics (ExAO, for ground-based observatories), non-common path aberration control (i.e. differential aberrations between sensing and science paths), diffraction suppression or coronagraphy, active optics (cophasing for segmented telescopes and regular active optics for all telescopes, e.g. telescope adaptive mirrors) and science image post-processing.

Pillars of high-contrast imaging at small angular separations include sophisticated techniques: amongst others,

* E-mail: mathilde.beaulieu@oca.eu

¹From www.exoplanets.eu.

(i) coronagraphic devices adapted to obstructed/segmented pupils and to small separation regimes (e.g. vortex coronagraph – Mawet et al. 2005; Foo, Palacios & Swartzlander 2005, phase-induced amplitude apodization – Guyon et al. 2010a) but at the cost of high sensitivity to aberrations;

(ii) deformable mirror (DM) technology for wavefront shaping. Rather than wavefront control, which flattens the wavefront errors from imperfect optics, wavefront shaping is the process of creating a dark zone (a so-called dark hole) in the PSF by locally minimizing the light in the focal plane. One limitation of wavefront shaping is the Fresnel propagation of phase aberrations (also called the ‘Talbot effect’): at the DM plane, out-of-pupil optics create a mix of amplitude and phase errors that a single DM can only correct at the expense of losing at least half of the field in the science image (e.g. Bordé & Traub 2006; Give’on et al. 2007). One way to deal with this effect is the use of at least two DMs to correct for both phase and amplitude over the full field;

(iii) quasi-static speckle calibration via post-processing, e.g. locally optimized combinations of images (LOCI, Lafrenière et al. 2007), observational strategies that benefit from the different behaviour of the planet and the star speckles, i.e. rotation angle (angular differential imaging, ADI, Marois et al. 2005), azimuthal spectral dispersion (spectral differential imaging, SDI, Marois et al. 2006a), spectrum (spectral deconvolution, SD, Sparks & Ford 2002) or polarization (polarization differential imaging, PDI, Kuhn, Potter & Parise 2001), and coherent differential imaging (CDI) that uses modulation to determine the coherent and incoherent parts of the field (i.e. Bordé & Traub 2006; Baudoz et al. 2006; Give’on et al. 2007).

Current observing sequences with, for instance, GPI (Macintosh et al. 2007), SPHERE (Beuzit et al. 2008), or SCEXAO (Guyon et al. 2010b) widely use reference PSF subtraction methods to improve high-contrast performance. However, those solutions are mostly inadequate at small angular separations where most of the starlight is concentrated, because of insufficient chromatic speckle elongation or field of rotation, etc. Improving the contrast performance at short separation imposes a reduction of the pupil plane wavefront errors with low spatial frequency to control the star energy distribution close to the optical axis in the science image. Speckle intensity in a coronagraphic image at close angular separation from the star is a highly non-linear function of wavefront errors that makes the situation very complex to tackle.

To date, the most advanced ground-based instruments (SPHERE, GPI, etc.) have yielded the discovery of fewer than five new exoplanets. Improving the level of detection of these instruments and/or anticipating the performance of new instruments in the ELT area can be achieved by (i) improving the correction of non-common path aberrations; (ii) improving the attenuation at a smaller inner working angle (IWA); (iii) improving the ExAO correction temporal frequency and sensitivity; and finally (iv) implementing sophisticated multi-DM wavefront shaping systems dedicated to dark-hole generation. Wavefront shaping systems have been tested in the laboratory (e.g. Lawson et al. 2013; Mazoyer et al. 2019) and on-sky (e.g. Savransky et al. 2012; Martinache et al. 2014; Bottom et al. 2016) but are not yet routinely implemented on on-sky instruments. From this perspective, the understanding of limiting parameters for high-contrast imaging at small separations is crucial and timely and has led to the development of various laboratory test beds and end-to-end simulations worldwide.

While laboratory set-ups have been developed to evaluate high-contrast imaging instrument technologies and concepts (e.g. SPEED

– the segmented pupil experiment for exoplanet detection, Martinez et al. 2014; HiCAT – the high-contrast imager for complex aperture telescopes, N’Diaye et al. 2013; HCST – the high-contrast spectroscopy test bed for segmented telescopes, Mawet et al. 2017; DST – the decadal survey test bed, Garrett et al. 2019; THD2 – *très haute dynamique*, Baudoz et al. 2018; and VODCA – the vortex optical demonstrator for coronagraphic applications, Jolivet et al. 2014), end-to-end numerical simulations are used to understand and predict high-contrast performance and limitations. The latter have been developed for instance for the WFIRST spatial mission (Krist, Nemati & Mennesson 2016), for LUVVOIR (Juanola-Parramon et al. 2019a), or for generic high-contrast instruments (Beaulieu et al. 2017). End-to-end simulator algorithms frequently include Fresnel propagators (Krist 2007) and/or energy minimization algorithms for dark-hole generation (Give’on et al. 2007; Pueyo et al. 2009; Riggs et al. 2018).

In particular, the end-to-end simulations developed in Beaulieu et al. (2017) aimed to determine the optimum wavefront control architecture for high-contrast imaging at small separations (around $1 \lambda/D$) using a combination of coronagraphy and wavefront shaping. The study assumed a generic high-contrast architecture with a perfect coronagraph, a monolithic circular aperture without any central obscuration or spiders, etc., to assess the impact of the location of the two DMs on wavefront shaping when assuming the Fresnel propagation of standard aberrated optics. The objective of the study was to restrict the analysis to the intrinsic properties of the optics set-up including polishing frequency distribution, relative beam size, the distance between optics, DM optical location (in a collimated beam – out-of-pupil plane or in a pupil plane – versus converging beam) and separation, and DM properties (actuator number, etc.). The analysis has shown that high-contrast imaging at small separations with multi-DM architectures requires large DM separations. In particular, a significant performance dependence on the DM location, on the aberration amount and power spectral density (PSD) power law and dark-hole size has been demonstrated.

The goal of the present paper is to provide a more realistic instrument set-up design to go further in the analysis by assessing the relative impact of set-up parameters (non-uniform source, residual pupil phasing aberrations, highly aberrated optics, realistic deformable mirrors, coronagraph, etc.) with a segmented and obstructed pupil.

Ideally, such an analysis is instrument-dependent and would require a case-to-case study. None the less, for the sake of generality and to derive guidelines for high-contrast imaging development, we use the SPEED test bed as a typical instrument for our study. The SPEED laboratory set-up is specifically intended for high-contrast imaging at very small angular separations with an ELT-like telescope simulator. SPEED includes a segmented and centrally obstructed primary mirror, cophasing optics, a coronagraph designed for small IWA with ELTs (a PIAACMC, phase-induced amplitude apodization complex mask coronagraph, Guyon et al. 2014), and a dual-DM wavefront shaping system. SPEED can be considered as representative of most of the current laboratory benches mentioned previously by sharing to some extent common optical system architectures, hardware, and/or observing strategies, though some objectives and parameters are different. The complexity of its optical design along with its numerous optics (25) and optics quality are typical to what current high-contrast instruments would incorporate apart from (i) the ExAO system and (ii) a few sub-systems required to interface with the telescope that are not relevant in a laboratory environment (derotator, atmospheric dispersion compensator, etc.), which are not taken into account. We use the sample of the SPEED set-up, but

we are interested in identifying fundamental limits for the entire field of exoplanet imaging (ground and space); thus our simulations are ‘turbulence free’ and go to contrasts congruent with a possible future space telescope. The current paper focuses on the challenging small separation regime (less than $2 \lambda/D$), in order to assess practical limitations to high-contrast imaging.

The general assumptions used for the analysis (speckle pattern modelling, dark-hole algorithm and numerical implementation) are described in Section 2. Section 3 describes the SPEED test bed and realistic assumptions used for the analysis whereas Section 4 shows the simulated effect on the contrast ratio performance. Finally, we provide a conclusion.

2 GENERAL ASSUMPTIONS

In this section, we describe the general assumptions on optics and we explain our numerical modelling methodology and dark-hole algorithm following the same formalism as for Beaulieu et al. (2017).

2.1 Speckle distribution modelling

The diffraction pattern in the science image results from the pupil shape, the aberration all along the test bed and the detector noises. For this analysis we have defined: (i) a segmented and obstructed pupil, which corresponds to the SPEED pupil and mimics the ELT features (see Section 3.2) and (ii) an optical set-up with static aberrations. We do not treat here quasi-static aberration as we assume that the correction time-scale is shorter than structural or thermal changes. The static aberration is simulated as followed: each optic is computed with random static aberrations defined by their total amount of aberration (in nm rms over the optic physical size) and their frequency distribution (power law of the power spectral density, PSD). We define each paraxial lens with standard optic qualities, i.e. with 5 nm rms aberration and a power law of the PSD in f^{-3} (typical to current manufacturing errors). For statistical analysis, 128 phase realizations are defined per optic and the performance is computed for each of the 128 cases. The statistical validity of using 128 realizations has been verified (Beaulieu et al. 2017). We do not treat detector noises (readout or current noises) or wavefront sensing errors in this paper.

2.2 Dark-hole algorithm

The analytical approach, based on the energy minimization, for generating a dark hole in the science image is described in Give’on et al. (2007), Pueyo et al. (2009), Groff (2012) and Beaulieu (2017), and is defined by computing the total energy at the image plane when assuming a first DM at the pupil plane and a second DM at an out-of-pupil plane. We resume here the formalism for clarity. We define:

- (i) E_0 as the initial aberrated field with amplitude A and phase φ ,
- (ii) C_1 as the linear operator from the pupil plane (where the first DM is located) to the focal plane,
- (iii) C_2 as the linear operator from the second DM (out-of-pupil plane) to the image plane,
- (iv) C_{12} as the linear operator from the first to the second DM plane,
- (v) a as the DM phases coefficients,
- (vi) g and h as the influence functions of respectively the first and second DMs.

We assume that all the phases are small enough to approximate $e^{i\varphi}$ by $1 + i\varphi$, and that $C_{12}[E_0 \cdot e^{i\varphi}]$ can be written in the form of $Ae^{i\phi}$

(and thus can be approximated by $A(1 + i\phi)$). The intensity inside the dark hole can be written as

$$I_{\text{DH}} = {}^t a M_0 a + 2 {}^t a \Im(b_0) + d_0, \quad (1)$$

where

$$\begin{aligned} M_0 &= G^* G, \\ G &= [G_1, G_2], \\ G_1 &= \begin{bmatrix} [C_1 \{A g_j\}]_i \end{bmatrix}, \\ G_2 &= \begin{bmatrix} [C_2 \{A h_j\}]_i \end{bmatrix}, \\ b_0 &= \begin{bmatrix} G_1^* C_1 \{E_0\} \\ G_2^* C_1 \{E_0\} \end{bmatrix}, \\ d_0 &= \langle C_1 \{E_0\}, C_1 \{E_0\} \rangle. \end{aligned}$$

M_0 represents the system response to each DM poke, b_0 represents the interaction between the DM and the aberration, and d_0 is the initial intensity with aberrations and flat DMs ($a = 0$). The solution

$$a = -M_0^{-1} \Im(b_0), \quad (2)$$

which represents the DM coefficients, minimizes the energy inside the dark hole. Other algorithms such as electric field conjugation (EFC, Give’on et al. 2007) and the stroke minimization method (Pueyo et al. 2009) optimize the contrast ratio and limit large stroke deviation. Because our model uses monochromatic light and assumes a perfect wavefront sensor, in our analysis, we do not handle large stroke deviation. We thus apply equation (2) without any stroke limitation.

2.3 Dark-hole numerical implementation

The dark-hole algorithm is implemented following Section 2.2 and is described in detail in Beaulieu et al. (2017). The interaction matrix M_0 is computed by first poking each DM actuator, then Fresnel-propagating the wavefront from the DM to the focal plane and finally recording the complex amplitude (we assume a perfect wavefront sensor). Because the DM surface solution is in phase (real DM stroke), we invert the real part of the matrix M_0 .

As illustrated in fig. 9 of Beaulieu et al. (2017), two iterative processes are necessary to optimize the DM coefficients. The first one concerns the inversion of the matrix M_0 that can lead to diverging solutions because of the presence of very low singular values. These are sorted from the highest to the lowest values to exclude some of them. The algorithm starts with the n first singular values from the singular value decomposition (and zeroing the remaining values) to compute the DM coefficients. Iteratively, the algorithm includes the next n singular values (previously zeroed), until the best contrast ratio is achieved. We empirically set the singular value threshold n to 5 because it represents a fair compromise between the performance and the computational time. In theory, applying the DM coefficients $a_{\text{th}} = -M_0^{-1} \Im(b_0)$ leads to the nominal theoretical intensity $I_{\text{th}} = {}^t a_{\text{th}} M_0 a_{\text{th}} + 2 {}^t a_{\text{th}} \Im(b_0) + d_0$. However, the small non-linearity of the optical operators C_1 , C_2 and C_{12} leads to a non-optimal solution ($I_{\text{DH}} \neq I_{\text{th}}$) and needs a second iterative process to optimize the contrast until the theoretical intensity I_{th} is reached.

The analysis presented in Beaulieu et al. (2017) has determined that high contrast at small separations requires large DM distances from the pupil but also small dark-hole sizes; we have thus defined the dark hole from 0.8 to 4 λ/D to emphasize performance at very

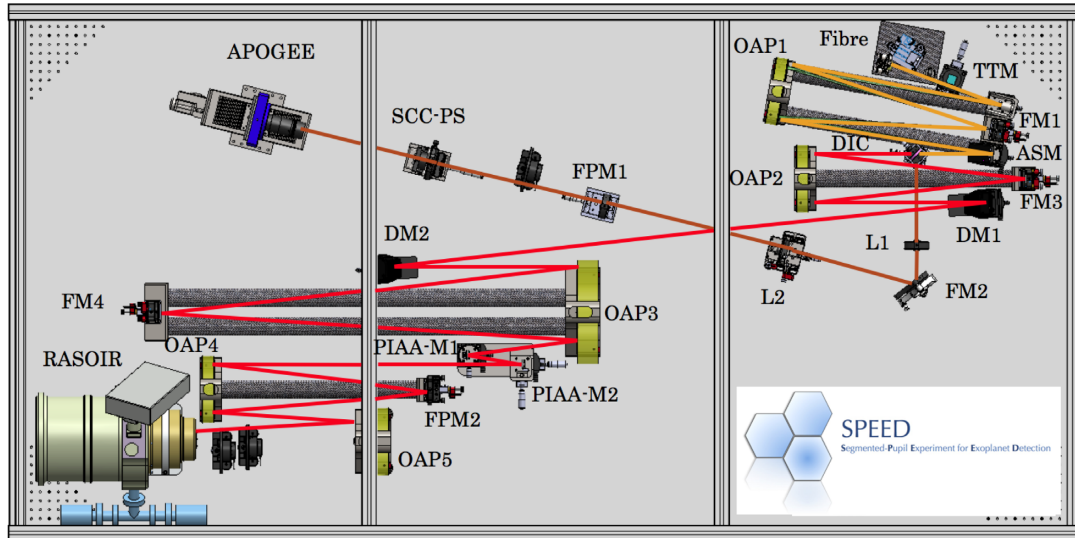


Figure 1. SPEED test bed. The common path (before the dichroic) is shown in orange, the visible path is represented in brown and the NIR path is in red. The acronyms on the figure are: L for lens, OAP for off-axis parabola, ASM for active segmented mirror, DM for deformable mirror, FM for flat mirror, DIC for dichroic, SCC-PS for self-coherent camera-phasing sensor, FPM for focal plane mask, PIAA-M1 and PIAA-M2 for the two PIAA mirrors for apodization, LS for Lyot stop, APOGEE for the visible camera and RASOIR for the NIR camera.

small separations. The code that we use for the Fresnel propagation between each optical element is PROPER (Krist 2007). PROPER and the dark-hole algorithm were written in IDL but translated into C++, such that the computation of the 128 configurations is performed simultaneously in a data centre available at the Observatoire de la Côte d’Azur to speed up the computational time (from one day to several hours for all the configurations).

3 REALISTIC OPTICAL SET-UP DEFINITION

This section introduces the optical set-up architecture and the working hypothesis that will offer an adequate playground for our study.

3.1 Generic high-contrast imaging model

Many worldwide high-contrast imaging test beds use several DMs for wavefront shaping (e.g. DST, HCST, HiCAT, SPEED, THD2). In particular, HiCAT, DST, HCST and SPEED incorporate a segmented and centrally obstructed pupil in their telescope simulators and thus implement closed-loop cophasing optics. Despite different objectives and parameters (different fields of view (FoV), coronagraphs, wavefront sensing methods, etc.), they share a common optical architecture consisting in ~ 25 optics, including the source module, a tip-tilt correction, a coronagraph, two (or more) DMs and off-axis parabolas (OAPs) to ensure the transition between pupil and focal planes. In this context, the SPEED test bed aims to achieve high contrast at very small separations in the H band with an ELT-like pupil, perfectly adapted to the problem of determining realistic limitations of high-contrast imaging at very small separations. This work focuses on the SPEED test bed (coronagraph, segmented/obstructed pupil, optical design, etc.) and the results can be applied to other high-contrast test beds because they share most of the set-up parameters.

3.2 The SPEED test bed

The SPEED test bed combines a source module and a telescope simulator (orange line), a dichroic reflecting the visible light to

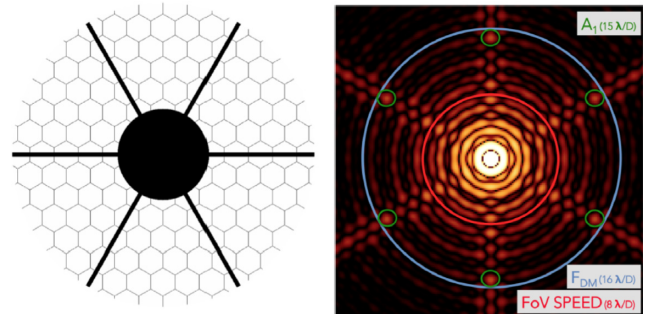


Figure 2. SPEED pupil (left) and corresponding FoV (right).

cophasing optics (brown) and transmitting the near-infrared light toward wavefront shaping, coronagraphy, and science camera (red). The bench layout and hardware are illustrated in Fig. 1. The test bed includes the following elements:

- (i) a *source module* made of a super-continuum light source feeding an optical fibre combined with a spherical mirror collimating the beam on to the tip-tilt mirror;
- (ii) a *tip-tilt mirror* to guarantee the stabilization of the PSF on the coronagraph;
- (iii) a *telescope simulator* combining an active segmented mirror (ASM) comprising 163 segments, controlled in piston and tip-tilt, and an optical mask inserted into the beam on the tip-tilt mirror to simulate a large central obscuration (30 per cent) and six spiders separated by 60 degrees. The pupil, shown on the left of Fig. 2, is 7.7 mm in diameter. The corresponding PSF is shown on the right of Fig. 2, illustrating the diffraction effects due to segmentation (green circles), the DM cut-off frequency (blue circle), and the defined SPEED FoV ($8 \lambda/D$, red circle);
- (iv) *cophasing sensors* including the self-coherent camera-phasing sensor (SCC-PS, Janin-Potiron et al. 2016) and alternatively a Zernike-based phasing sensor (Janin-Potiron et al. 2017);

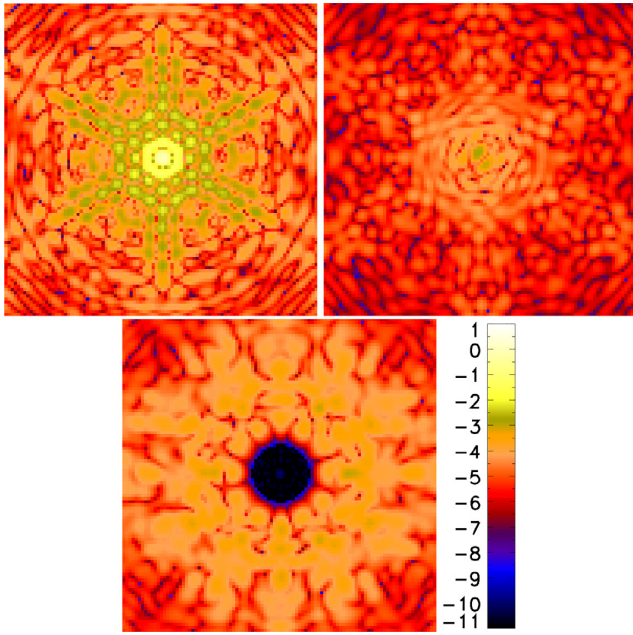


Figure 3. Contrast ratio images in logarithmic scale before the coronagraph (top left) and after the coronagraph and before (top right) and after (bottom) the dark-hole algorithm. The overall figure represents $44\lambda/D$ in size.

(v) *a wavefront shaping system* combining two continuous facesheet DMs from Boston Micromachine.² The DMs are made of 34×34 actuators with an inter-actuator pitch of $300 \mu\text{m}$. The two DMs are located at 1.5 and 0.2 m on both sides of the pupil plane, to maximize the performance between 0.8 and $4 \lambda/D$ (Beaulieu et al. 2017);

(vi) *a PIAACMC* offering high throughput and a small IWA of $1 \lambda/D$. The PIAACMC combines three elements: a lossless apodization with aspheric mirrors to weaken the Airy rings, a phase-shifting focal plane mask, and a Lyot stop that blocks the diffracted light. The design, specifications and manufacturing of the coronagraphic prototype are detailed in Martinez et al. (2014);

(vii) *an infrared camera* operating at a wavelength of $1.65 \mu\text{m}$ with a 1k by 1k Hawaii detector array.

3.3 Realistic simulations

End-to-end simulators have been developed with various objectives and complementary analysis; we here focus on a few of them. In Krist et al. (2011) (developed as part of the technology demonstration for exoplanet missions and applied to the WFIRST mission) the authors compare the performance of different coronagraphs in polychromatic light when taking into account the propagation of both phase and amplitude errors on each optic. On the other hand, in Beaulieu et al. (2017), we statistically analyse the impact of phase errors on the performance in monochromatic light and at very small separations assuming a perfect coronagraph. Finally, in Juanola-Parramon et al. (2019a) the authors determine the impact of the telescope aberration on the performance in polychromatic light for the LUVOIR mission assuming perfect instrument optics and an APLC (Apodized Pupil Lyot Coronagraph) coronagraph.

In the current paper, we present the relative impact of set-up parameters on the ability to efficiently control phase and amplitude

²<http://www.bostonmicromachines.com>

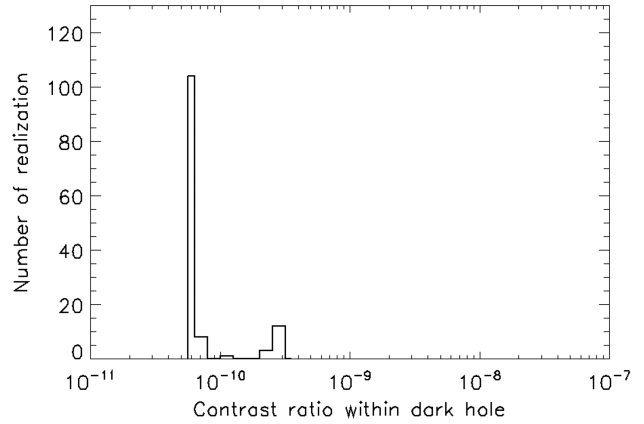


Figure 4. Nominal 5σ contrast ratio histogram within the dark hole (from 0.8 to $4 \lambda/D$). The simulation assumes the SPEED set-up at $1.65 \mu\text{m}$, a perfectly cophased mirror, a theoretical PIAACMC coronagraph and two DMs with infinite stroke located 0.2 and 1.5 m from the pupil plane.

to create dark holes at very small separations (around $1 \lambda/D$) when taking into account Fresnel propagation of standard optics errors but also specific and realistic optical set-up parameters. We consider in our analysis three main categories of errors: (i) phase errors that are not taken into account in the nominal case: highly aberrated optics (e.g. deformable mirror windows), residual phase aberrations on the segmented pupil, or coronagraph realistic manufacturing errors; (ii) amplitude errors due to the source module such as segment reflectivity variation or missing segments in the pupil; (iii) errors from the active correction system itself such as stroke limitation or a non-functional actuator.

4 NUMERICAL RESULTS

This section describes the impact of realistic parameters (previously defined in Section 3.3) on the performance. The performance criteria are defined as the 5σ contrast ratio histogram computed for each of the 128 random realizations. This corresponds to the number of random realizations that achieve a given contrast ratio inside the defined dark hole (see Section 4.1 for illustration purposes). The numerical pupil diameter size is 225 pixels corresponding to the 7.7 mm pupil diameter for a grid size of 1024 pixels. The simulation is monochromatic at the wavelength of $1.65 \mu\text{m}$.

4.1 Nominal case

We define a nominal case as a comparison basis to assess the relative impact of each parameter. It corresponds to a 25 optics set-up containing: (i) an obscured mask with spiders located on a tip-tilt mirror, (ii) a perfectly cophased segmented mirror (with 163 segments), (iii) a theoretical PIAACMC coronagraph, and (iv) two DMs (34×34 actuators) with infinite stroke located 1.5 and 0.2 m from the pupil plane.

The nominal case assumes 5 nm rms aberration with a PSD in f^{-3} for each passive optic including the dichroic and the DM windows. These parameters are used in the rest of the paper unless specified otherwise. For illustration purposes, Fig. 3 shows an example of the achieved contrast ratio images: initial (top left) and coronagraphic before (top right) and after (bottom) the dark-hole algorithm. The plot on Fig. 4 shows the contrast ratio histogram, representing the number of realizations (ordinate) that reach a given 5σ contrast (abscissa, in

logarithm scale) defined as the median of the contrast computed within a dark hole from 0.8 to $4 \lambda/D$ from the optical axis.

Because our simulations assume a perfect wavefront sensor and preclude amplitude and temporal errors, the algorithm reaches very high contrast (nominal 5σ contrast ratio of 6.10^{-11}), well below what real instruments can achieve. None the less, this nominal contrast ratio serves as a reference, showing that some of the optical parameters not appropriately set can degrade the contrast level to a limiting value.

4.2 Phase errors

4.2.1 Analytical description and interpretation

The correction of an aberrated optic by a dual-DM system depends on both the dark-hole spatial frequencies and the optic location to the DM position. If the DM correction frequency and the aberrated optic frequency distributions are not adapted, the correction will be inefficient. In this section, we determine the limitation in correction induced by an aberrated optic at a given location.

Following the same rationale and formalism as for Beaulieu et al. (2017), we briefly recall here the main equations. An out-of-pupil optic creates at the focal plane a sine and cosine modulation as

$$E_f(x', y') = \frac{e^{i\frac{2\pi}{\lambda}(2f-z)}}{i\lambda f} \times \eta \times \widehat{E_{\text{opt}}}(u, v), \quad (3)$$

with

$$\eta = \cos\left(\frac{\pi\lambda z}{D^2}(x'^2 + y'^2)\right) + i \sin\left(\frac{\pi\lambda z}{D^2}(x'^2 + y'^2)\right), \quad (4)$$

and where $\widehat{}$ represents the Fourier transform, E_f is the electric field at the focal plane, E_{opt} is the electric field in the optic plane, u and v are the spatial coordinates at the optic plane, D is the pupil diameter, λ is the wavelength, f is the imaging camera focal length, z is the distance of the optic to the pupil plane and x' and y' are the spatial frequencies expressed in $\frac{\lambda}{D}$. This modulation impacts the real (cosine) and imaginary (sine) parts of η and contributes to the correction efficiency.

We first consider the case where the optic is a DM ($\eta = \eta_{\text{DM}}$). The modulation then impacts the stroke amplitude as low sine or cosine values need to be compensated by a large DM stroke, which could be out of the algorithm linear regime assumption for energy minimization, and even out of the DM correction range. We illustrate this impact by showing in Fig. 5 the absolute values of the sine contribution for three DM locations (0.2 m in black, 1.5 m in red and 3 m in blue) for a beam diameter of 7.7 mm and an imaging wavelength of $1.65 \mu\text{m}$. The sine term (or similarly the cosine term) oscillates and thus degrades the overall system efficiency over the spatial frequencies. In particular, the sine contribution at small separations (below $4 \lambda/D$) is efficiently covered by a DM located at a large distance (> 1 m, blue and red curves) but not by a DM at a small distance (black curve). By applying the same rationale for the cosine term and by taking into account the second DM (see Beaulieu et al. 2017 for details), the DM locations have been defined to optimize the sine and cosine terms between 0.8 and $4 \lambda/D$, corresponding to DM locations of 1.5 and 0.2 m from the pupil plane.

We now consider the case where the optic is an out-of-pupil aberrated window. The electric field at the focal plane is also modulated (equation 3) and needs to be corrected by the DMs. The correction efficiency depends on the DM modulation: if the DM modulation (sine or cosine term of η_{DM}) is low at the frequencies

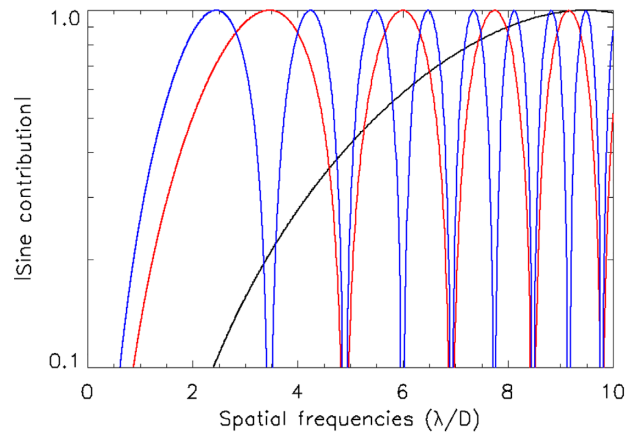


Figure 5. Sine contribution as a function of the dark-hole frequencies for different DM locations: 0.2 (black), 1.5 (red) and 3 m (blue) from the pupil plane.

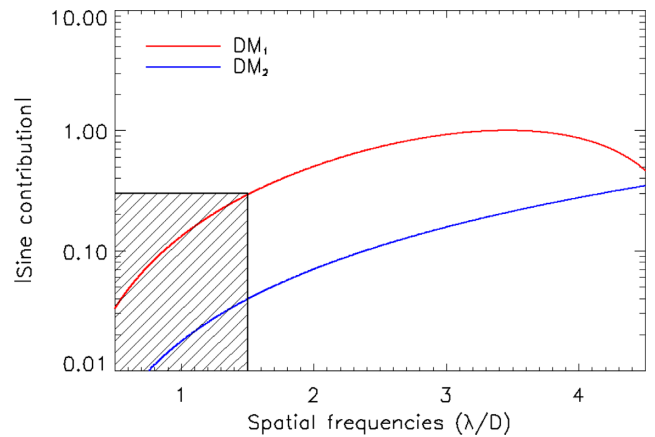


Figure 6. Sine contribution of DM₁ (red) and DM₂ (blue). If the DM correction is low (dark region, sine values less than 30 percent), an out-of-pupil aberrated optic will be inefficiently corrected.

where the window's modulation is high, the correction will be inefficient. We first focus on the sine contribution. This is illustrated in Fig. 6, which shows, for the previously defined DMs (DM locations of 1.5 and 0.2 m from the pupil plane), the two DM sine contributions (red and blue curves) as a function of the spatial frequencies in λ/D . The dark hatched region corresponds to a low-efficiency regime, where the sine contribution of both DMs is low (arbitrarily defined as a sine value less than 30 percent, i.e. where the DM₁ and DM₂ contributions are both lower than 30 percent).

The impact of an out-of-pupil aberrated window is determined by the contribution of this optic where the DMs are not efficient. This is the value of the window sine contribution at the frequencies where the DM contribution is below 30 percent. We thus define the degradation of correction by the mean of the window sine contribution, for frequencies where the DM contribution is low (dark hatched region of Fig. 6). This degradation term is a qualitative indicator that must be complemented by the contrast ratio estimation with end-to-end simulation. The same rationale is applied to the cosine term of η in equation (4). Nevertheless, with the previously chosen DM locations (0.2 and 1.5 m from the pupil plane), there is no region where the cosine contributions of both DMs are less than 30 percent, leading to a good coverage of the real part of η_{DM} .

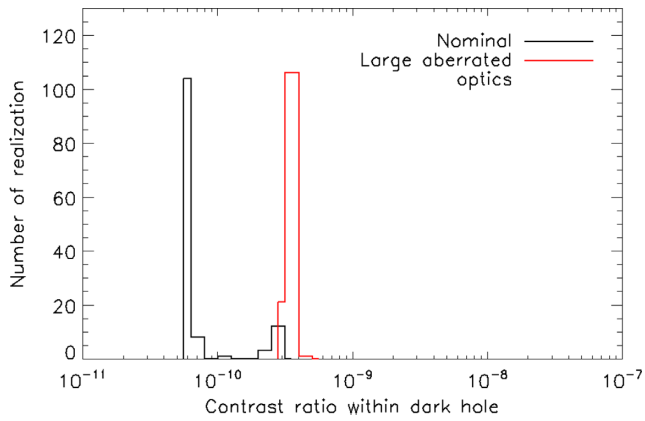


Figure 7. Impact on 5σ contrast ratio of aberrated optics located in a collimated beam.

This approach is based on the DM correction degradation due to the location of an aberrated optic, i.e. the DM correction efficiency when taking into account the Talbot effect (Fresnel propagation). However, this method does not distinguish the aberrations located before and after the coronagraph.

4.2.2 Impact of aberrated optics in collimated beam

We assess the impact of aberrated optics located in a collimated beam (for instance, the dichroic and the DM windows), referred as to near-pupil-plane aberrations, even though one DM is located 1.5 m from the pupil plane. The aberration amount is based on realistic manufacturing data, i.e. 20 nm rms for the dichroic (standard $\lambda/10$ surface quality), 30 nm rms for the DM windows and 50 nm rms for the active segmented mirror window (standard $\lambda/4$ surface quality). Each mirror window is simulated twice to take the mirror reflection into account, leading to an overall amount of aberrations of 95 nm rms. The impact on performance is shown in Fig. 7. Despite the large amount of aberration introduced by these optics, the contrast ratio remains high (the 5σ contrast ratio is degraded to 3.10^{-10}), corresponding to an efficient DM correction. The DM window aberrations, as they are located at the DM planes, are obviously well corrected by the DMs themselves. The impact of the dichroic is quantitatively explained by the analytical approach discussed in Section 4.2.1: by computing the degradation on correction (defined in Section 4.2.1) in this case, we find that the DM location is appropriate to correct for this optic aberration (degradation of correction values below 0.05).

4.2.3 Impact of near-focal-plane aberrated optics

We here appraise the impact of a standard aberrated window (5 nm rms, PSD in f^{-3}), located near the detector plane (e.g. a cryostat window). We simulate the performance when adding aberrated optics located at 1, 2, 3, 4, 5, 10, 20, 30, 40 and 50 per cent of the camera focal length (corresponding to df in the layout of Fig. 8). For clarity, the results are shown on two different plots. The top plot of Fig. 9 corresponds to df values of 5, 10, 20, 30, 40 and 50 per cent of the focal length whereas the plot on the bottom corresponds to df values from 1 to 5 per cent of the focal length. We notice a performance degradation when the aberrated optic is located near the focal plane (5 to ~ 30 per cent of the focal length; see top panel), compared to larger locations (> 30 per cent) but the contrast ratio is not affected for optics located very close to the focal plane (from 1 to 4 per cent

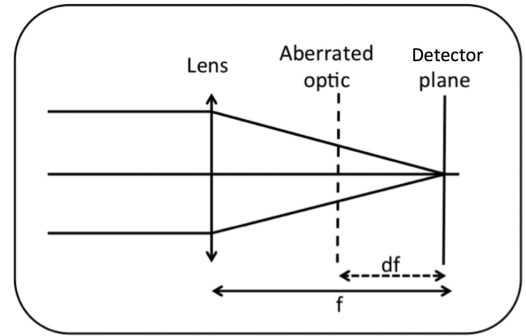


Figure 8. Illustration of simulation layout: aberrated optics located at df values of 1, 2, 3, 4, 5, 10, 20, 30, 40 and 50 per cent of the focal length.

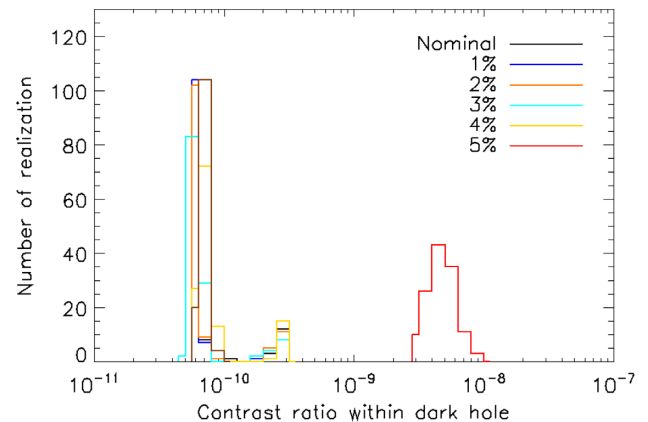
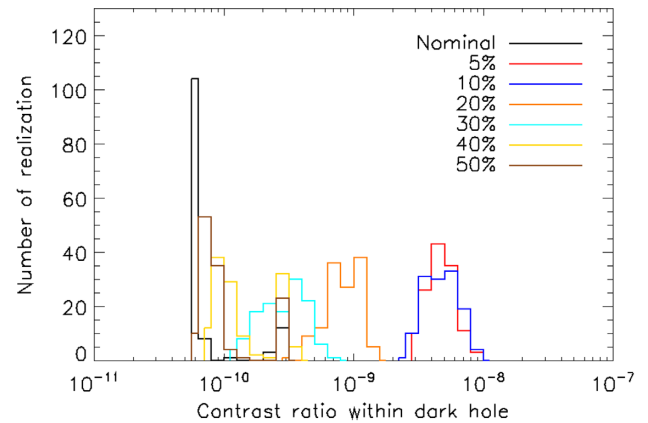


Figure 9. 5σ contrast ratio histogram for aberrated optics at df values of 5, 10, 20, 30, 40 and 50 per cent of the focal length (top) and from 1 to 5 per cent of focal length (bottom).

of the focal length; see bottom panel). As an illustration, 5 per cent of the focal length corresponds to 30 mm and 30 per cent corresponds to 180 mm for the SPEED test bed.

To grasp these results, we follow the same rationale as in Section 4.2.1. An aberrated window located near the focal plane can be considered as the image, formed by a lens, of an object located in the collimated beam. We thus compute, for each df position, the geometrical location of the corresponding object in the collimated beam, and thus the corresponding distance z to the pupil plane (equations 3 and 4). The degradation of correction defined

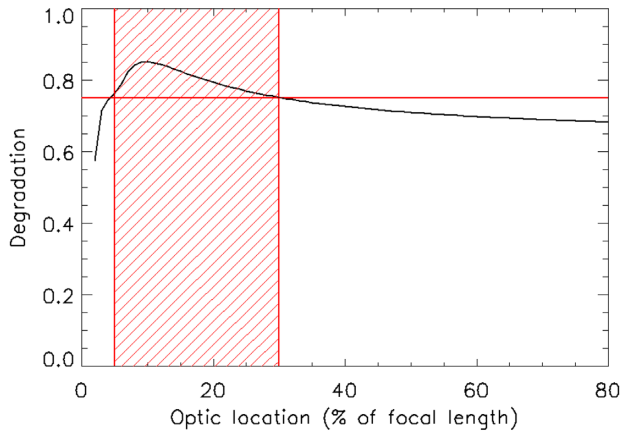


Figure 10. Degradation in DM correction due to aberrated optic, as a function of the optic location in per cent of focal length.

in Section 4.2.1 is finally computed for each case and is shown in Fig. 10, where we notice two contrast performance regimes. The first regime corresponds to the region where the simulated contrast ratio is significantly degraded, i.e. for df values between 5 and 30 per cent (see Fig. 9) where the degradation is highest (greater than 0.75; see the red hatched region of Fig. 10). The second regime is the region exhibiting limited contrast ratio degradation, where the degradation is lower than 0.75. Thus, the previous back-of-an-envelope degradation estimation of Section 4.2.1 can be used as a baseline to determine the impact in a contrast ratio of near-focal-plane windows or optics but end-to-end simulation is needed for quantitative estimates. In future work we could consider implementing an estimation of these aberrations (Paul et al. 2013) or a non-linear approach (Pueyo & Norman 2013; Paul et al. 2013) to mitigate this effect.

Moreover, while the degradation from 40 to 5 per cent is progressive (from a contrast ratio of $\sim 10^{-10}$ to $\sim 5.10^{-9}$ in the top panel of Fig. 9), the impact for df values less than 5 per cent is binary (contrast ratio of 5.10^{-9} or $\sim 5.10^{-11}$). Although the trend is well explained by the analytical approach of Section 4.2.1, these dichotomic values can be explained by the propagator code: PROPER (Krist 2007) uses the angular spectrum and the Fresnel approximation as propagation algorithms and automatically determines which one is the best to implement from the ratio between the propagation distance and the Rayleigh distance. The transition between the two approaches is physically progressive but numerically dichotomous to avoid sampling issues. In the simulated case, the transition between the near- and far-field approaches is precisely between 4 and 5 per cent, explaining the dichotomy in the contrast ratio values at those values.

We also note an analogy with the effect described in Marois, Phillion & Macintosh (2006b) that determines the impact in polychromatic light of optics close to the focal plane in the simultaneous spectral differential imaging efficiency (SSDI, Smith 1987; Rosenthal, Gurwell & Ho 1996; Racine et al. 1999; Marois et al. 2000). Marois et al. (2006b) evaluate how the Talbot effect due to out-of-pupil plane optics impacts the SSDI speckle-noise reduction and show that near-focal-plane aberrations can significantly degrade the performance. Our study determines that, even for the monochromatic case, the effect of near-focal-plane optics is not negligible on high-contrast imaging with wavefront shaping and should be taken into account during instrument development.

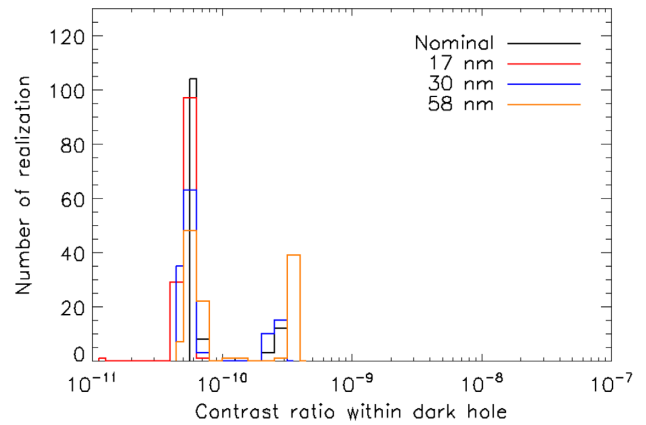


Figure 11. Contrast ratio (5σ) histogram when taking into account 17 nm rms aberrations (10 nm defocus, 10 nm piston and 10 nm tip-tilt, in red), 30 nm rms aberrations (10 nm defocus, 20 nm piston and 20 nm tip-tilt, in blue), and 58 nm rms (10 nm defocus, 40 nm piston and 40 nm tip-tilt, in orange).

These end-to-end simulations, combined with the analytical description discussed in Section 4.2.1, illustrate the impact of aberrations in the DM correction depending on their location. Whereas the previous analysis was realized for optics near the detector plane, it can be generalized to each test-bed focal plane, upstream or downstream of the coronagraph. It is generally accepted, in the field of astronomical instrumentation, that optics aberrations upstream of the coronagraph are more detrimental than optics aberrations downstream of the coronagraph. The current results determine that, even for optics located after the coronagraph, the DM correction can be inefficient.

4.2.4 Impact of phasing residuals

In this section, we assume the presence of cophasing errors left uncorrected by the phasing unit. Because we focus on realistic laboratory test beds, we exclude on-sky observation errors that interact with cophasing optics (i.e. low-wind effect, XAO residuals, etc.). We simulate manufacturing and alignment errors resulting in low-order aberrations (piston, tip-tilt, and focus error on each segment). Segment defocus, which cannot be corrected by cophasing optics, is defined as 10 nm rms, which is consistent with the SPEED ASM phase map measured in the laboratory. We simulate the impact of cophasing errors on piston and tip-tilt through three cases: with 10, 20, and 40 nm rms per aberration type (piston and tip-tilt). The resulting overall aberration amounts (piston, tip-tilt, plus defocus) are respectively 17, 30 and 58 nm rms. Those values are conservative as for SPEED we expect nearly zero residual errors in a few cophasing algorithm iterations (Janin-Potiron et al. 2016, 2017). As an illustration, the HiCAT test bed achieves a residual phasing surface error of 9 nm rms (Soummer et al. 2019). The impact on performance (5σ contrast ratio) is presented in Fig. 11 and shows no impact on achieved contrast.

Previous simulations point out lower tolerance in cophasing errors: the study for LUVOIR, presented in Juanola-Parramon et al. (2019a), shows that a contrast ratio of $\sim 10^{-10}$ can be achieved with 1 nm rms telescope aberration (piston and tip-tilt) and with wavefront control with two DMs. Even if it does account for the impact of a more aberrated primary mirror on the performance, it seems to be a strong constraint for high-contrast achievement. This difference in high-

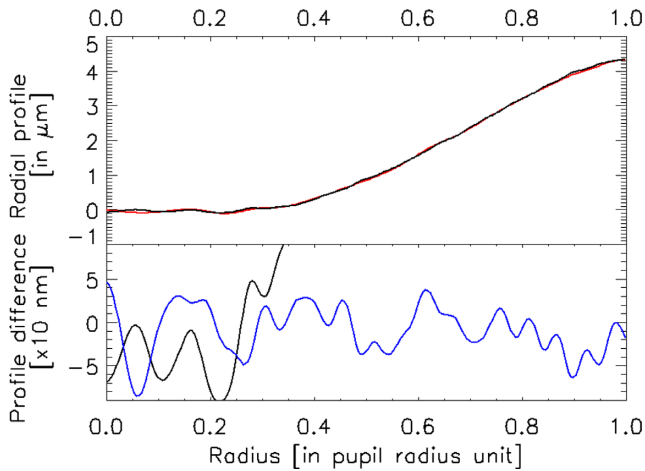


Figure 12. SPEED PIAACMC first mirror profile on top: theoretical profile (black curve in the top plot) and with 30 nm rms simulated manufacturing errors (red curve in the top plot). The profile difference between the theory and simulated manufacturing errors is in blue in the bottom plot whereas the theoretical profile is over-plotted in black.

contrast limitation can be explained by: (i) a monochromatic analysis (the study in Juanola-Parramon et al. 2019a considers polychromatic light), leading the algorithm to converge in a easier and more efficient way. Furthermore, the impact of aberration is reduced in the current analysis, as the simulation is in the H band (versus in the visible in Juanola-Parramon et al. 2019a) and the impact of aberration error is reduced at larger wavelengths; (ii) the dark-hole size is smaller in our analysis (overall size of $3.2\lambda/D$ versus $8.5\lambda/D$ in Juanola-Parramon et al. 2019a), relaxing the strain on DM frequencies and thus allowing more flexibility; and (iii) the LUVUOIR optics distances and sizes are much larger than those for the SPEED project (spatial telescope versus laboratory test bed), leading to larger Fresnel propagation effects.

4.2.5 Impact of coronagraph manufacturing errors

The PIAACMC consists of two aspheric mirrors to geometrically apodize the beam, a focal plane mask (FPM), and a Lyot stop. The PIAACMC components have been designed to meet the small IWA performance constraints with an ELT-like pupil (30 per cent central obscuration ratio, six spiders at 60°), in a monochromatic set-up at $1.65 \mu\text{m}$. This has led to the definition of two centrally symmetric mirrors for the apodization and a multi-zone phase-shifting FPM consisting in ~ 500 hexagons of $25 \mu\text{m}$ diameter with depths (optical path differences) from -0.4 to $0.4 \mu\text{m}$. As described in Martinez et al. (2018), those optimized optics lead to a theoretical IWA of $1.3 \lambda/D$ and a raw contrast of 10^{-5} at IWA. We here simulate optical aberrations on the PIAACMC components to evaluate the impact on performance.

Several PIAACMC FPMs have been recently manufactured (i.e. Kern et al. 2016; Newman et al. 2016; Knight et al. 2017; Martinez et al. 2019). Manufactured depth errors represent typically a few per cent of the peak-to-valley value of the sag. We thus simulate an FPM sag error of 5 nm rms, consistent with the SPEED FPM manufacturing tolerance analysis (Martinez et al. 2018) and with the prototype characterization (Martinez et al. 2019).

We also simulate aberrations on the PIAACMC aspheric mirrors, following the defined specification: a sag deviation (best effort) of 25 nm rms (Martinez et al. 2018). We thus simulate two cases

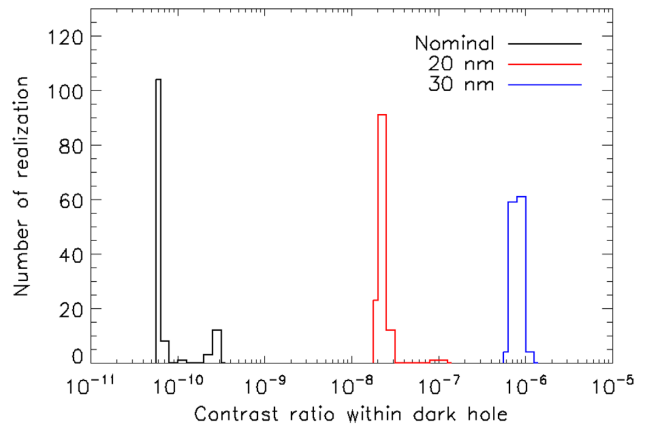


Figure 13. 5σ contrast ratio histogram assuming the simulated FPM and aspheric aberrations. The FPM is simulated with 5 nm rms aberration and the aspheric mirrors are simulated with 20 (red) and 30 (blue) nm rms.

corresponding to sag deviations of 20 and 30 nm rms, divided into low and middle frequencies, to keep smoothed mirror profiles. The top part of Fig. 12 illustrates the simulated SPEED PIAACMC first mirror profile (the theoretical one in black and with simulated manufacturing errors of 30 nm rms in red). The difference between the two profiles corresponds to the blue curve in the bottom plot of Fig. 12 (the theoretical profile is over-plotted in black).

The FPM and aspheric manufacturing errors have been simulated separately, showing very low impact when adding the FPM manufacturing errors and a major contribution of the aspheric mirror errors. Fig. 13 represents the contrast ratio resulting in an FPM sag deviation of 5 nm rms plus aspheric mirror sag deviations of 20 nm rms (in red) and 30 nm rms (in blue), showing the major impact of aspheric errors.

Although the aspheric mirrors are located in a collimated beam, we note a major degradation in performance for 30 nm rms errors, in contradiction with the discussion in Sections 4.2.1–4.2.3. This can be explained by contrast degradation due to coronagraphic manufacturing errors: whereas FPM manufacturing errors are located at the focal plane and impact the overall sag, aspheric mirror manufacturing errors can impact the profile at high frequencies. The theoretical profile in the top part of Fig. 12 shows high-frequency ripples located at radii less than 0.4 pupil radius. Manufacturing errors of the same order of magnitude as the ripples (see the bottom part of Fig. 12) will directly degrade the coronagraph performance. The DMs will not be able to correct for this effect as long as the ripple frequencies are higher than the DM cut-off frequency and/or the DM locations are not optimized to correct for those frequencies.

4.3 Amplitude errors

4.3.1 Impact of non-uniform pupil illumination

The source module has been simulated using a realistic polychromatic optical fibre numerical aperture (NA) of ~ 0.2 in the H band. This NA range of value creates a non-uniform pupil unless the focal length of the relay optic is sufficiently large to intercept only the ‘top-hat’ of the fibre Gaussian profile, but at the price of creating a Fresnel pattern due to the large propagated distance. We thus simulate separately the impact of a non-uniform pupil profile coming from these two cases: (i) a non-uniform Gaussian profile due to the fibre

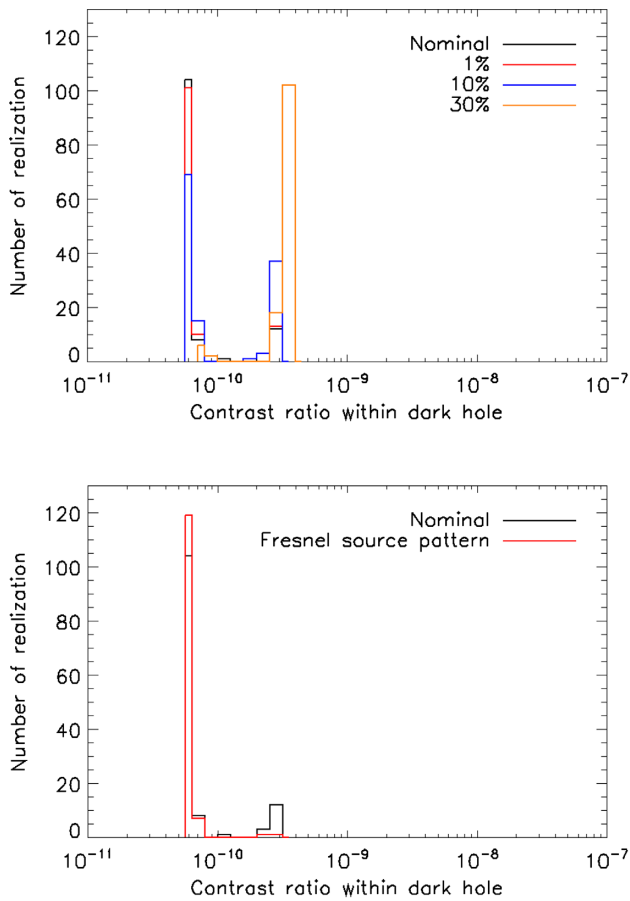


Figure 14. Impact of a Gaussian non-uniform (1, 10 and 30 per cent) pupil (top) and of a Fresnel non-uniform pupil (bottom) on performance (5σ contrast ratio).

NA, and (ii) a non-uniform Fresnel pattern due to large propagation distances.

The fibre Gaussian profile is simulated assuming 1, 10 and 30 per cent non-uniformity in amplitude on the overall pupil (from the top to the centre of the pupil profile). The impact of such non-uniformity is shown in the top panel of Fig. 14: a non-uniformity lower than 10 per cent does not affect the performance as it is corrected by the two DMs.

The Fresnel propagation pattern is simulated assuming the same optical fibre NA (~ 0.2 in the H band) and a focal length sufficiently large (~ 600 mm) to create a quasi-uniform (few per cent) profile (‘top-hat’ of the Gaussian) on the overall pupil. The impact on performance (5σ histogram) is shown in the bottom panel of Fig. 14. We do not see any impact of such a profile on the contrast ratio performance.

We can observe that the amplitude errors from non-uniform pupil illumination are well corrected by the system. The wavefront shaping is efficient because of the dual-DM architecture (which corrects for both phase and amplitude errors) and the amplitude error localization (near the pupil plane).

4.3.2 Impact of ASM missing segments

In this section, we investigate the impact of a few ASM non-functional segments on the performance. We choose to study one

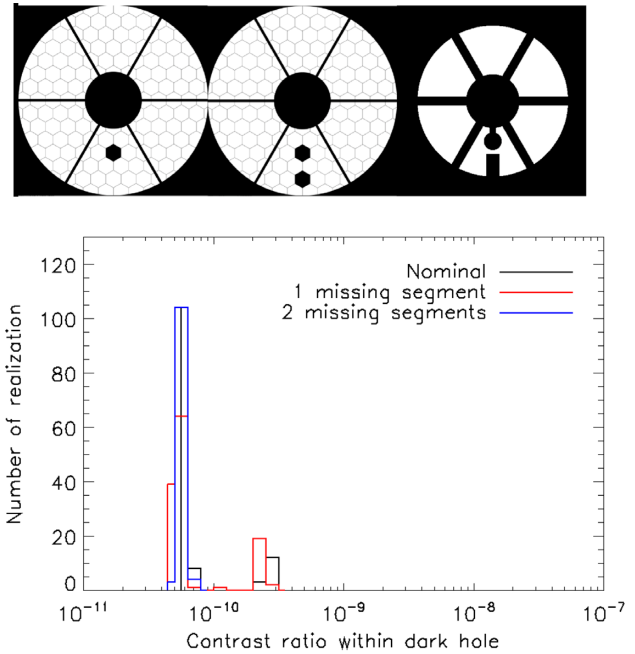


Figure 15. Pupil with one (top left) and two (top centre) missing segments and adapted Lyot stop for the two missing segments cases (top right). The impact on performance is shown in the bottom panel.

of the worst cases, where the missing segments are not obstructed by the spiders, for the sake of generality. Fig. 15 shows the results for one (top left) and two missing segments (top centre). The Lyot stop is designed to cover the missing segments for each case (e.g. top right). We observe no impact on the 5σ contrast ratio (bottom).

No major impact on performance is observed when increasing the number of missing segments while adapting the Lyot stop. Even though we see no significant impact, ASM missing segments can impact the performance, by degrading the cophasing correction level and modifying the overall instrument transmission and signal-to-noise ratio (SNR).

4.3.3 Impact of ASM reflectivity variation

We consider the effect of segment reflectivity variations by analysing the impact of three configurations: (i) a mean reflectivity of 99 per cent over the pupil with a variation of ± 1 per cent, (ii) a mean reflectivity of 95 per cent with a variation of ± 5 per cent, and (iii) a mean reflectivity of 90 per cent with a variation of ± 10 per cent. Results are shown on Fig. 16, where reflectivity variations less than 10 per cent do not significantly impact the contrast, illustrating that the locations of the two DMs lead to efficient error correction at the pupil plane (see Section 4.2.2). While missing segments and segment reflectivity variations create speckles in the coronagraphic image, these static errors are well corrected by the active optic because we use a dual-DM architecture and because the errors are localized at the pupil plane, where the wavefront shaping is efficient.

4.4 Errors from the active correction system

4.4.1 Impact of deformable mirror finite stroke

We assess the impact of DM stroke precision in the dark-hole algorithm efficiency. The algorithm was adapted to consider the

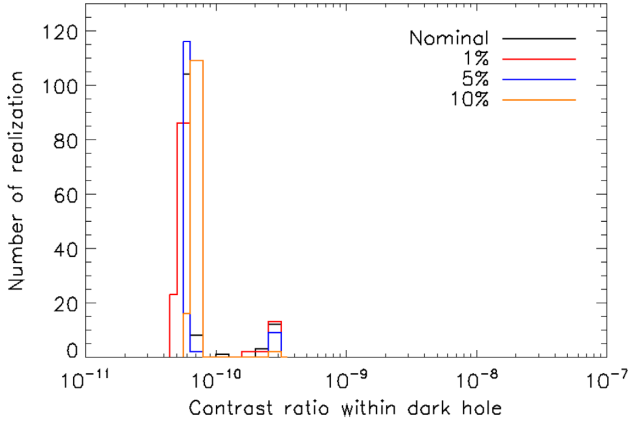


Figure 16. 5σ contrast ratio histogram for the nominal case (black) and for segment reflectivity variations of 1, 5, and 10 per cent in red, blue, and orange, respectively.

smallest step that an actuator can achieve. This DM stroke precision is evaluated from the manufacturer’s data. The deflection curve (deflection versus voltage) and the driver precision (14 bits) lead to a maximum stroke precision of 0.25 nm with an average of 0.15 nm. We thus study the impact of representative stroke precision values (of 0.1, 0.2 and 0.5 nm) on the contrast performance. For simplicity, in the rest of the analysis, we assume that this stroke precision value is the same for each actuator of the two DMs.

The degradation in contrast ratio due to finite stroke was described in Jiang et al. (1991) and Trauger et al. (2011). As a rule of thumb, Trauger et al. (2011) define the contrast floor due to DM fitting error as $\sim \pi \frac{(8\sigma)^2}{(n\lambda)^2}$. This value can be computed by assuming a wavefront corrected at n locations (n defined as the DM actuator number) over the aperture diameter with a stroke precision defined as σ_0 . For simplicity, we assume a DM located at the pupil plane. The fitting error variance over the whole aperture (defined as $\mathcal{A} = \pi n^2/4$) is thus $\sigma_{\text{err}} = 4\sigma_0^2/(\pi n^2)$. The corresponding electric field at the focal plane is

$$E_f \approx \widehat{A}(u, v) + iA(u, v)\widehat{\phi}(u, v) \approx iA(u, v)\widehat{\phi}(u, v), \quad (5)$$

when assuming small phase and a set-up with a coronagraph that removes (or significantly attenuates) the constant term A . The phase ϕ is defined as $2 \times \frac{2\pi}{\lambda} \sigma_{\text{err}}$ assuming a reflective (mirror) surface. We can write the contrast inside the dark hole using the Parseval theorem by

$$\mathcal{C}_{\text{DH}} \approx \left(2 \times \frac{2\pi}{\lambda}\right)^2 \sigma_{\text{err}}^2 \approx \pi \frac{(8\sigma_0)^2}{(n\lambda)^2}, \quad (6)$$

in accordance with Trauger et al. (2011). Equation (6) leads to contrast floor values of 6.10^{-10} , 2.10^{-9} , and 2.10^{-8} for stroke precision values of 0.1, 0.2, and 0.5 nm, respectively. The 5σ contrast ratio histograms for stroke precision values of 0.1, 0.2, and 0.5 nm are shown in Fig. 17. As illustrated in Table 1, the means of the achieved 5σ contrasts are 5.10^{-9} , 2.10^{-8} , and 9.10^{-8} , and correspond to median contrast values of 7.10^{-10} , 2.10^{-9} , and 1.10^{-8} , consistent with the theoretical values of 6.10^{-10} , 2.10^{-9} and 2.10^{-8} . Whereas equation (6) assumes a single DM configuration at the pupil plane, it estimates fairly well the contrast limitation due to finite stroke in the case of two out-of-pupil plane DMs.

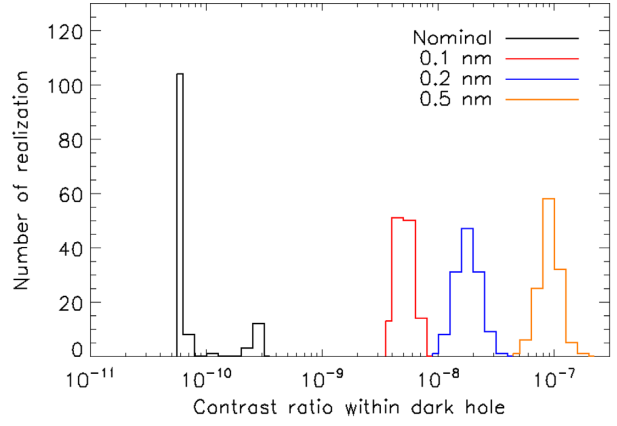


Figure 17. Contrast ratio (5σ) histogram when taking into account 0.1, 0.2, and 0.5 nm finite stroke.

Table 1. Theoretical and achieved contrast ratio for stroke precisions of 0.1, 0.2, and 0.5 nm. The theoretical mean contrast is computed from equation (6) at $1.65 \mu\text{m}$ with $n = 34$ actuators.

Stroke precision	Theoretical mean contrast	Achieved mean contrast	Achieved 5σ contrast
0.1 nm	6.10^{-10}	7.10^{-10}	5.10^{-9}
0.2 nm	2.10^{-9}	2.10^{-9}	2.10^{-8}
0.5 nm	2.10^{-8}	1.10^{-8}	9.10^{-8}

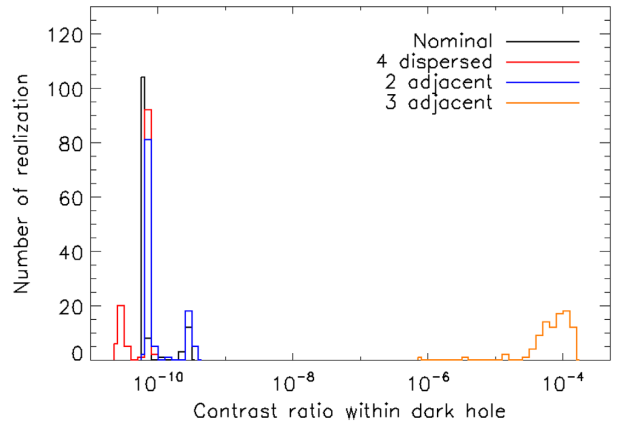


Figure 18. Contrast ratio (5σ) histogram when taking into account one (red curve), two (blue curve) non-functional actuators on one DM or one non-functional actuator per DM (orange curve).

4.4.2 Impact of deformable mirror non-functional actuators

We appraise the impact of non-functional actuators on the deformable mirrors for the wavefront shaping, as illustrated in Fig. 18. We simulate the impact in two cases: when the dead actuators are dispersed over the DM (dispersed actuators, red curve) or adjacent (two or three grouped actuators for the blue and orange curves). The deformable mirrors are located out of the pupil plane, at a large distance from the pupil plane, such that the image of a dead actuator is *diluted* at the Lyot stop plane, precluding the use of an adapted Lyot stop to prevent this effect. This also explains that the performance is less affected by dead actuators scattered over the DM than adjacent actuators (where the impact is less *diluted*).

Table 2. Impact of each simulated parameter on the 5σ contrast ratio.

Parameter	5σ contrast ratio
Nominal	6.10^{-11}
Phase errors	
Aberrated windows in collimated beam	3.10^{-10}
Aberrated windows near the science detector (5–30% of focal length)	$> 10^{-9}$
Aberrated windows near the science detector (1–4% or 30% of focal length)	$< 10^{-9}$
Phasing residual wavefront error	$< 5.10^{-10}$
Realistic PIAACMC coronagraph with 20 nm rms on aspheric mirrors	2.10^{-8}
Realistic PIAACMC coronagraph with 30 nm rms on aspheric mirrors	8.10^{-7}
Amplitude errors	
Non-uniform source (if $< 10\%$)	6.10^{-11}
ASM non-functional segments with adapted Lyot stops	6.10^{-11}
ASM reflectivity variation	$< 5.10^{-10}$
Correction errors	
DM stroke 0.1 nm	5.10^{-9}
DM stroke 0.2 nm	2.10^{-8}
DM stroke 0.5 nm	9.10^{-8}
Three adjacent non-functional actuators	10^{-4}

Matthews et al. (2017) analysed the impact of DM damaged actuators on the simulated performance of Project 1640. The authors simulated some damaged actuators on a DM located at the pupil plane and showed low contrast degradation for randomly distributed and dispersed dead actuators (zero stroke value). Our analysis shows the same low degradation for dispersed actuators but also demonstrates the impact of grouped dead actuators on performance.

We also simulated this impact with a larger dark hole (from 2 to $5 \lambda/D$). It showed the same degradation trend, illustrating that this impact is not inherent to the small-separation–high-contrast paradigm.

5 CONCLUSION AND DISCUSSION

In Beaulieu et al. (2017), we demonstrated that imaging at small angular separations requires a large set-up and a small dark-hole size. The analysis only considered the wavefront shaping system parameters such as the number of actuators, the deformable mirror locations, and the optic aberrations (level and frequency distribution). In that context, we used an ideal and generic high-contrast architecture with a perfect coronagraph, a monolithic circular aperture without any central obscuration or spiders, etc. In the present study, we have extended the former study to a more realistic set-up, combining a segmented and obstructed telescope pupil with a real coronagraph (PIAACMC). We have also included: (i) phase aberrations such as aberrated optics located in a collimated beam (e.g. DM windows or dichroic) or near the focal plane (e.g. camera cryostat window), telescope phasing residuals or coronagraph manufacturing errors; (ii) amplitude errors such as non-uniform pupil illumination, primary mirror missing segments and segment reflectivity variations; and (iii) errors originating from the wavefront shaping system itself (finite stroke and non-functional actuators). We have simulated the impact of these realistic parameters on the contrast ratio at very small separations (around $1 \lambda/D$).

We summarize the impact of each item on the performance in Table 2, where the most limiting parameters are written in bold for the sake of clarity. We notice that a highly aberrated optic does not impact the performance as long as it is located in a

collimated beam (cophasing errors, deformable mirror windows, dichroic). We also found that one or two missing segments can be compensated by adapting the Lyot stop accordingly. We have identified some major constraints to high contrast at small separations that, to our knowledge, were not identified in previous analyses. Some of these constraints come from the corrected system itself (coronagraph and deformable mirror). For instance, finite DM stroke and adjacent non-functional actuators, as well as phase errors on the coronagraph or near the focal plane, are a major limitation to high-contrast imaging at small separations. They significantly degrade the contrast ratio (arbitrarily set to a degradation of 1000). More specifically, in the astronomical instrumentation community, a clear dichotomy is widely accepted between optics aberrations upstream and downstream of the coronagraph. Our study clearly demonstrates that optics aberrations downstream of the coronagraph cannot be neglected. They will severely impact the wavefront shaping performance otherwise.

We demonstrate that the contrast limit due to the DM stroke as predicted by equation (6) (Trauger et al. 2011) is fairly valid. We propose a methodology (see Section 4.2.1) to estimate the correction efficiency in the presence of the aberrated window location, regardless of its position on the optical design. We note that this conclusion is valid for the SPEED set-up, and especially for the PIAACMC coronagraph, even if the SPEED optical model is representative of high-contrast imaging test beds. An end-to-end simulation of a high-contrast set-up is always needed to assess the expected contrast value. None the less, the parameters studied in this analysis can be used as a baseline to assess some major limitations for high-contrast imaging at small separation, for ground- or space-based instrumentation or for other test beds. We demonstrate that achieving high contrast below $2 \lambda/D$ is challenging and needs an appropriate set-up.

In future work, we will continue to improve the realism of our end-to-end modelling by adding realistic wavefront sensor and detector noises. We also aim at testing (i) the non-linear dark-hole approach (Pueyo & Norman 2013; Paul et al. 2013) and in particular if it can compensate for non-functional actuators and (ii) broad-band performance. More peculiar and recent sources of errors could also be envisioned as well, such as the petal phase offset (N’Diaye et al. 2018) and the low-wind effect (Sauvage et al. 2016). Because of the intrinsic faintness of low-mass exoplanets, integration time will be on the order of hours; the stability of the dark hole over these time-scales is critical, and quasi-static speckles will need to be treated as well.

ACKNOWLEDGEMENTS

The authors are grateful to the computing centre personnel for their support.

DATA AVAILABILITY

The data underlying this article will be shared on reasonable request to the corresponding author.

REFERENCES

- Baudoz P., Boccaletti A., Baudrand J., Rouan D., 2006, in Aime C., Vakili F., ed., IAU Colloq. 200, Direct Imaging of Exoplanets: Science Techniques, p. 553
- Baudoz P., Galicher R., Potier A., Dupuis O., Thijs S., Patru F., 2018, in Proc. SPIE, Volume 10706, Advances in Optical and Mechanical Technologies for Telescopes and Instrumentation III, p. 1070620
- Beaulieu M., 2017, PhD thesis, Univ. Côte d’Azur

- Beaulieu M., Abe L., Martinez P., Baudoz P., Gouvret C., Vakili F., 2017, *MNRAS*, 469, 218
- Beuzit J.-L. et al., 2008, in Proc. SPIE, Volume 7014, Ground-based and Airborne Instrumentation for Astronomy II. p. 701418
- Bolcar M. R. et al., 2018, in Proc. SPIE, Volume 10698, Space Telescopes and Instrumentation 2018: Optical, Infrared, and Millimeter Wave. p. 106980O
- Bordé P. J., Traub W. A., 2006, *ApJ*, 638, 488
- Bottom M., Femenia B., Huby E., Mawet D. C., Dekany R., Milburn J., Serabyn E., 2016, in Proc. SPIE, Volume 9909, Adaptive Optics Systems V. p. 990955
- Foo G., Palacios D. M., Swartzlander G. A., Jr, 2005, *Opt. Lett.*, 30, 3308
- Garrett R., Crill B., Patterson K., Mejia C., Seo B., Siegler N., 2019, https://exoplanets.nasa.gov/internal_resources/1170/
- Gaudi B. S. et al., 2018, preprint (arXiv:1809.09674)
- Give'on A., Kern B., Shaklan S., Moody D. C., Pueyo L., 2007, in Proc. SPIE, Volume 6691, Astronomical Adaptive Optics Systems and Applications III. p. 66910A
- Groff T. D., 2012, PhD thesis, Princeton Univ.
- Guyon O., Martinache F., Belikov R., Soummer R., 2010a, *ApJS*, 190, 220
- Guyon O., Martinache F., Garrel V., Vogt F., Yokochi K., Yoshikawa T., 2010b, in Proc. SPIE, Volume 7736, Adaptive Optics Systems II. p. 773624
- Guyon O., Martinache F., Cady E. J., Belikov R., Balasubramanian K., Wilson D., Clergeon C. S., Mateen M., 2012, in Proc. SPIE, Volume 8847, Adaptive Optics Systems III. p. 84471X
- Guyon O., Hinz P. M., Cady E., Belikov R., Martinache F., 2014, *ApJ*, 780, 171
- Janin-Potiron P., Martinez P., Baudoz P., Carbillot M., 2016, *A&A*, 592, A110
- Janin-Potiron P., N'Diaye M., Martinez P., Vigan A., Dohlen K., Carbillot M., 2017, *A&A*, 603, A23
- Jiang W., Ling N., Rao X., Shi F., 1991, in Ealey M. A., in Proc. SPIE, Volume 1542, Active and Adaptive Optical Systems. p. 130
- Jolivet A., Piron P., Huby E., Absil O., Delacroix C., Mawet D., Surdej J., Habraken S., 2014, in Proc. SPIE, Volume 9151, Advances in Optical and Mechanical Technologies for Telescopes and Instrumentation. p. 91515P
- Juanola-Parramon R., Zimmerman N. T., Groff T., Pueyo L., Rizzo M., Bolcar M., Roberge A., 2019a, in American Astronomical Society, AAS Meeting #233. p. 148.06
- Juanola-Parramon R., Zimmerman N. T., Pueyo L., Bolcar M., Ruane G., Krist J., Groff T., 2019b, in Proc. SPIE, Volume 11117, Techniques and Instrumentation for Detection of Exoplanets IX. p. 1111705
- Kern B. et al., 2016, *J. Astron. Telesc. Instrum. Syst.*, 2, 011014
- Knight J. M., Brewer J., Hamilton R., Ward K., Milster T. D., Guyon O., 2017, in Proc. SPIE, Volume 10400, Techniques and Instrumentation for Detection of Exoplanets VIII. p. 104000N
- Krist J. E., 2007, in Proc. SPIE, Volume 6675, Optical Modeling and Performance Predictions III. p. 66750P
- Krist J. E., Belikov R., Pueyo L., Mawet D. P., Moody D., Trauger J. T., Shaklan S. B., 2011, in Proc. SPIE, Volume 8151, Techniques and Instrumentation for Detection of Exoplanets V. p. 81510E
- Krist J., Nemati B., Mennesson B., 2016, *J. Astron. Telesc. Instrum. Syst.*, 2, 011003
- Krist J. et al., 2019, in Proc. SPIE, Volume 11117, Techniques and Instrumentation for Detection of Exoplanets IX. p. 1111702
- Kuhn J. R., Potter D., Parise B., 2001, *ApJ*, 553, L189
- Lafrenière D., Marois C., Doyon R., Nadeau D., Artigau É., 2007, *ApJ*, 660, 770
- Lawson P. R. et al., 2013, in Proc. SPIE, Volume 8864, Techniques and Instrumentation for Detection of Exoplanets VI. p. 88641F
- Macintosh B. et al., 2007, in American Astronomical Society, AAS Meeting #211. p. 782
- Marois C., Doyon R., Racine R., Nadeau D., 2000, *PASP*, 112, 91
- Marois C., Doyon R., Racine R., Nadeau D., Lafreniere D., Vallee P., Riopel M., Macintosh B., 2005, *J. R. Astron. Soc. Canada*, 99, 130
- Marois C., Lafrenière D., Doyon R., Macintosh B., Nadeau D., 2006a, *ApJ*, 641, 556
- Marois C., Phillion D. W., Macintosh B., 2006b, in Proc. SPIE, Volume 6269, p. 62693M
- Martinache F. et al., 2014, *PASP*, 126, 565
- Martinez P. et al., 2014, in Proc. SPIE, Volume 9145, Ground-based and Airborne Telescopes V. p. 91454E
- Martinez P., Beaulieu M., Guyon O., Abe L., Gouvret C., Dejonghe J., Preis O., 2018, in Proc. SPIE, Volume 10702, Ground-based and Airborne Instrumentation for Astronomy VII. p. 1070243
- Martinez P. et al., 2019, *A&A*, under press
- Matthews C. T., Crepp J. R., Vasisht G., Cady E., 2017, *J. Astron. Telesc. Instrum. Syst.*, 3, 045001
- Mawet D., Riaud P., Absil O., Surdej J., 2005, *ApJ*, 633, 1191
- Mawet D. et al., 2017, *ApJ*, 838, 92
- Mazoyer J. et al., 2019, Astro2020: Decadal Survey on Astronomy and Astrophysics, APC white papers
- N'Diaye M. et al., 2013, in Proc. SPIE, Volume 8864, Techniques and Instrumentation for Detection of Exoplanets VI. p. 88641K
- N'Diaye M., Martinache F., Jovanovic N., Lozi J., Guyon O., Norris B., Ceau A., Mary D., 2018, *A&A*, 610, A18
- Newman K., Conway J., Belikov R., Guyon O., 2016, *PASP*, 128, 055003
- Paul B., Mugnier L., Sauvage J.-F., Dohlen K., Ferrari M., 2013, *Opt. Express*, 21, 31751
- Pueyo L., Norman C., 2013, *ApJ*, 769, 102
- Pueyo L., Kay J., Kasdin N. J., Groff T., McElwain M., Give'on A., Belikov R., 2009, *Applied Opt.*, 48, 6296
- Pueyo L. et al., 2019, in Proc. SPIE, Volume 11117, Techniques and Instrumentation for Detection of Exoplanets IX. p. 1111703
- Racine R., Walker G. A. H., Nadeau D., Doyon R., Marois C., 1999, *PASP*, 111, 587
- Riggs A. J. E., Ruane G., Sidick E., Coker C., Kern B. D., Shaklan S. B., 2018, in Proc. SPIE, Volume 10698, Space Telescopes and Instrumentation 2018: Optical, Infrared, and Millimeter Wave. p. 106982V
- Rosenthal E. D., Gurwell M. A., Ho P. T. P., 1996, *Nature*, 384, 243
- Sauvage J.-F. et al., 2016, in Proc. SPIE, Volume 9909, Adaptive Optics Systems V. p. 990916
- Savransky D., Macintosh B. A., Thomas S. J., Poyneer L. A., Palmer D. W., De Rosa R. J., Hartung M., 2012, in Proc. SPIE, Volume 8447, Adaptive Optics Systems III. p. 84476S
- Smith W. H., 1987, *PASP*, 99, 1344
- Soummer R. et al., 2019, in Proc. SPIE, Volume 10698, Space Telescopes and Instrumentation 2018: Optical, Infrared, and Millimeter Wave. p. 106981O
- Sparks W. B., Ford H. C., 2002, *ApJ*, 578, 543
- Trauger J., Moody D., Gordon B., Krist J., Mawet D., 2011, in Proc. SPIE, Volume 8151, Techniques and Instrumentation for Detection of Exoplanets V. p. 81510G

This paper has been typeset from a $\text{\TeX}/\text{\LaTeX}$ file prepared by the author.